machines

MDPI

Article

Modified Induction Machine Equivalent Circuit Including Solid Shaft Eddy Currents

Didem Tekgun

Department of Electrical and Electronics Engineering, Abdullah Gul University, Kayseri 38080, Turkey; didem.tekgun@agu.edu.tr

Abstract: The shaft eddy currents cause a significant saturation in two-pole induction machines (IMs) as they generate an opposing field and repulse the main flux, thus tightening the flux path. This results in inaccurate performance estimations with the magnetizing inductance measured in no-load conditions when the machine is loaded. This article presents a modified IM equivalent circuit considering the rotor back iron saturation effects caused by the solid shaft eddy currents using experimental measurements and recursive parameter estimation techniques. The classical equivalent circuit (CEC) parameters are determined with the standard test techniques followed by the parameter estimation of the newly introduced modified equivalent circuit (MEC) parameters. The proposed modified equivalent circuit is benchmarked with CEC and finite element analysis (FEA) simulations with and without considering eddy effects. The proposed MEC model and the FEA that consider eddy effects performed better than the other models and yielded a negligibly small error over a wide range of loading conditions. Compared to the FEA, the proposed MEC estimates the IM performance much faster, which makes it more appealing for IM performance estimations.

Keywords: two-pole induction machine; solid shaft; modified equivalent circuit; FEA

Citation: Tekgun, D. Modified Induction Machine Equivalent Circuit Including Solid Shaft Eddy Currents. *Machines* **2023**, *11*, 1090. https://doi.org/10.3390/machines11121090

Received: 24 October 2023
Revised: 10 December 2023
Accepted: 14 December 2023
Published: 15 December 2023

1. Introduction

Induction machines (IMs) are the favorite choice in a wide range of applications, from various industrial applications to high-performance electric vehicles, due to their simple, cost-effective, robust structures. Also, being able to start with AC mains directly is a feature that IMs have, which makes them more attractive over synchronous machines in many applications [1].

Although over 90% of the motors used in the world are IMs, they suffer from low efficiency and power factor (PF) compared to synchronous machines [2,3]. The PF is an important performance metric that plays a key role in determining the motor powers, output torque, and efficiency. Hence, estimating the PF accurately is important to calculate the performance of the motor, which is dictated by international standards with strict tolerances [4].

IMs are mostly made of two, four, and six poles depending on the application's torque density and speed requirements [5]. For applications that require high speed when running at 50–60 Hz line frequency, two-pole IM is a suitable choice as it can operate over 2500 rev/min speeds when fully loaded [3].

Two-pole AC machines have a flux path where the flux crosses the rotor from one side to the opposite side. Usually, magnetic materials like ST45 1040–1045 structural steels are used as shaft materials for the flux to also travel through the shaft [6]. In case the shaft is selected as a nonmagnetic material, two-pole machines saturate quickly and start to draw higher magnetizing current, which results in thermal issues and increased copper and core losses [7,8].

Since the shaft is a solid steel material that has no laminations, and the IM rotor currents have slip frequency, the shaft experiences eddy currents circulating through the

axial direction [9]. Consequently, these eddy currents generate an opposing field and force the main rotor flux to pass through the rotor back iron, thus causing a bottleneck on the flux path. As a result, the rotor back iron starts to saturate as the flux is forced to travel through the rotor back iron. The saturation level merely depends on the loading condition and the rotor geometry. This effect is more significant in two-pole induction machines with longer axial lengths and large shaft diameters [10,11].

The field disturbing effect of the solid shaft-related eddy currents is investigated in the literature with various analytical, finite element analysis (FEA), improved equivalent circuit methods, and a combination of these analysis methods [12–17]. Among these methods, the FEA method takes longer computation time but generates accurate results [18,19]. On the other hand, analytical methods save significant computation time but yield high estimation errors, especially when the saturation level is high and the rotor has non-uniform geometric entities like cooling vents [9]. Various hybrid performance estimation methods are also proposed to achieve faster computation time and acceptable accuracy at rated operating conditions [15,19].

The equivalent circuit model studies in the literature consider the classical equivalent circuit model parameters to be tuned around the operating point. In [19], an improved equivalent circuit approximation is presented where the motor parameters are tuned iteratively using the FEA analysis results. However, the performance degrades when the loading varies as the saturation effect is not considered in the classical equivalent circuit model.

This paper presents a modified equivalent circuit (MEC) model to cope with the saturation effects due to the solid magnetic shaft eddy currents. Different from the existing literature, the proposed model considers the rotor back iron saturation in the equivalent circuit caused by the shaft eddy currents. A new magnetizing branch that represents the additional saturation effect of the rotor parallel to the magnetizing inductance, along with the eddy current loss resistance series to the rotor branch, is introduced due to the fact that an increase in the slip, rotor current amplitude and frequency are increased. Hence, the eddy currents flowing in the solid shaft increase and result in higher saturation on the rotor back iron. Accordingly, the magnetizing inductance is assumed to be a combination of the stator and rotor magnetizing inductances that are connected in parallel. The rotor magnetizing inductance is modeled as a function of the slip, while the stator magnetizing inductance is modeled as a scaled magnetizing inductance. To determine the motor classical equivalent circuit parameters, the locked rotor test and no-load tests are conducted. Later, load tests are performed at various operating points, and test data are collected for modified circuit parameter determination. Loading test data contain the phase current, PF, and torque variations with respect to the slip while the supply voltage is kept constant. The new parameter coefficients are predicted using a recursive estimation technique by inputting the experimental test results into the estimation system.

A two-pole, 5.5 HP IM is considered for testing the efficacy of the proposed modified circuit. A close correlation is observed between the performance estimations of the MEC model and the experimentally measured values. Later, the proposed method is applied to five different IE1—standard efficiency IMs at various power levels, and similar estimation performances are observed.

The rest of the paper is organized as follows: The physics behind the problem is explained in Section 2. The proposed modified equivalent circuit model is introduced in Section 3. The parameter determination and estimation of the new circuit components are explained in Section 4. Section 5 provides the simulation and experimental results and discussion. Finally, the concluding remarks are provided in Section 6.

2. Problem Definition

To explain the effect of the shaft eddy currents phenomenon, a set of FEA simulations are conducted on a 400 V, 50 Hz, wye-connected, two-pole, 5.5 HP squirrel cage induction machine whose geometric parameters are detailed in Figure 1 and Table 1.

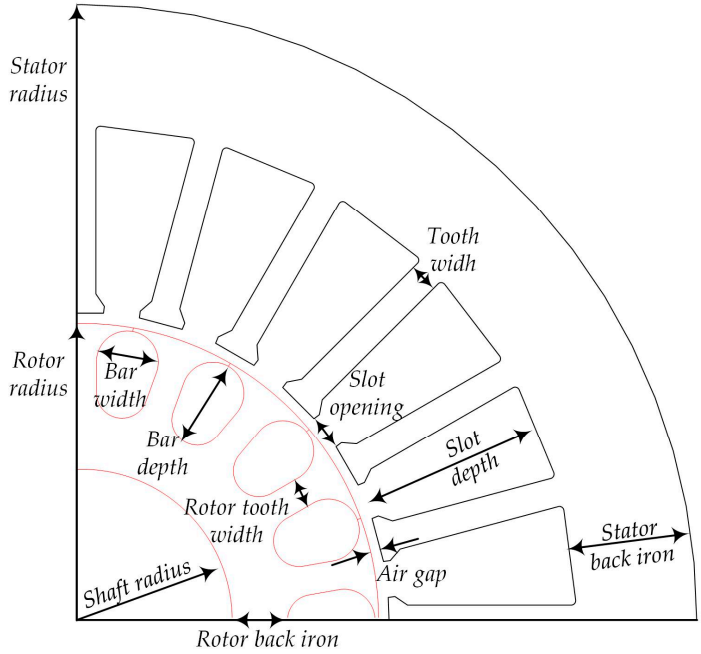

Figure 1. Geometric parameters of the machine.

Table 1. Details of the machine parameters.

Parameter	Value
Stator slot number	24
Rotor slot number	18
Stator radius	67 mm
Rotor radius	33.25 mm
Shaft radius	32 mm
Air gap	0.7 mm
Stator slot opening	3.7 mm
Stator back iron	14.05 mm
Rotor back iron	6.25 mm
Stator tooth width	3.3 mm
Rotor tooth width	3.5 mm
Stator slot depth	19 mm
Rotor bar depth	11 mm
Rotor bar width	6.7 mm
Stack length	148 mm
Number of turns per slot	41

Here, the FEA simulations are conducted in the ANSYS/Maxwell 2023 R1 software package, where transient analysis is performed with the rated line voltage fed to the windings. The speed is provided as a controlled variable; hence, a constant slip can be provided to the simulation. Figure 1 presents the steady state results at 200th msec, which is after 10 consecutive electric cycles. Since the machine operates at steady state conditions, the pictured instant of the rotor flux and density will only rotate after this instant. The loading is controlled with the slip variation between 0 and 10% in Figure 2.

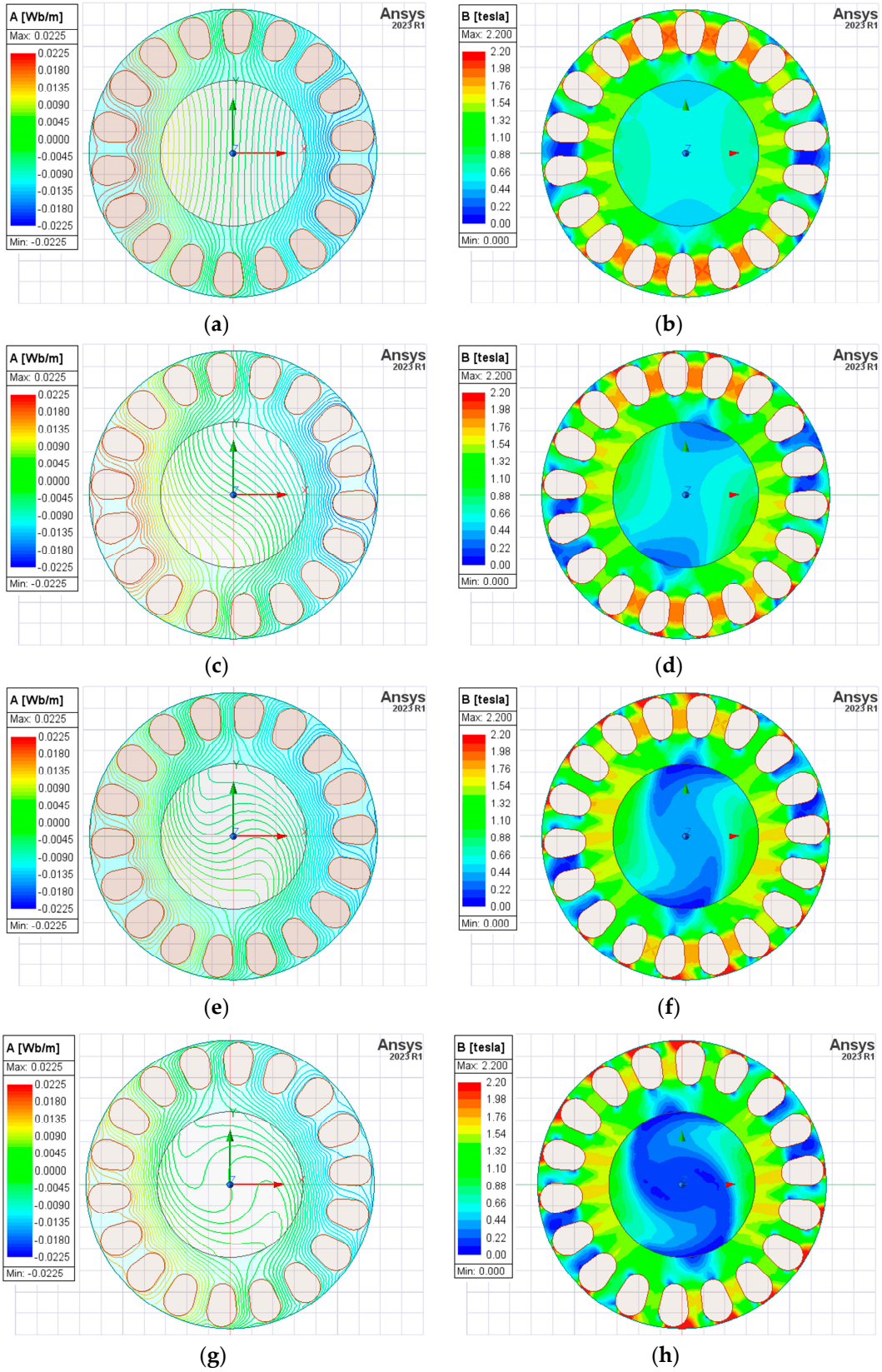

Figure 2. IM flux and flux density variations with the slip value increase from 0 to 10%, where the (**a**) zero slip (3000 rev/min speed) flux and (**b**) flux density; (**c**) 3% slip (2910 rev/min speed) flux and (**d**) flux density; (**e**) 6% slip (2820 rev/min speed) flux and (**f**) flux density; (**g**) 10% slip (2700 rev/min speed) flux and (**h**) flux density.

The two-pole AC machine shaft is considered an active magnetic section where a decent amount of rotor flux passes through it. When a two-pole IM runs at no-load condition, the slip and the rotor currents are negligibly small. Thus, negligible rotor flux is confined to the shaft core, where it mostly flows through the laminated rotor core that has a lower reluctance, as shown in Figure 2a. Here, the slip and speed are taken as 0 and 3000 rev/min. As the machine is loaded and the rotor speed slows down, the slip and the rotor current frequency and amplitude increase, which results in more eddy currents circulating in the shaft. These eddy currents generate their magnetic field, which partially repels the main flux from the shaft and even from the inner side of the rotor back iron [20].

Figure 2c,e,g show how the rotor flux path changes due to the fields that eddy current generated when the speed varies from 2910 rev/min to 2700 rev/min, where slip varies between 3% and 10%. Consequently, the flux path becomes narrower while the flux amplitude increases, and eventually, the rotor back iron starts to saturate, as shown in Figure 2b,d,f,h.

Figure 3 illustrates the flux density distribution when the slip is 10%, with and without the eddy current effect. In Figure 3a, flux density exceeds 1.7 T at some spots where the rotor back iron becomes narrower. However, the flux density is around 1.5 T and below for a large amount of back iron area. In Figure 3b, flux density exceeds 1.7 T at some spots but stays around 1.6 T and above in a wide rotor back iron area. The level of saturation is obviously higher when shaft eddy currents are present.

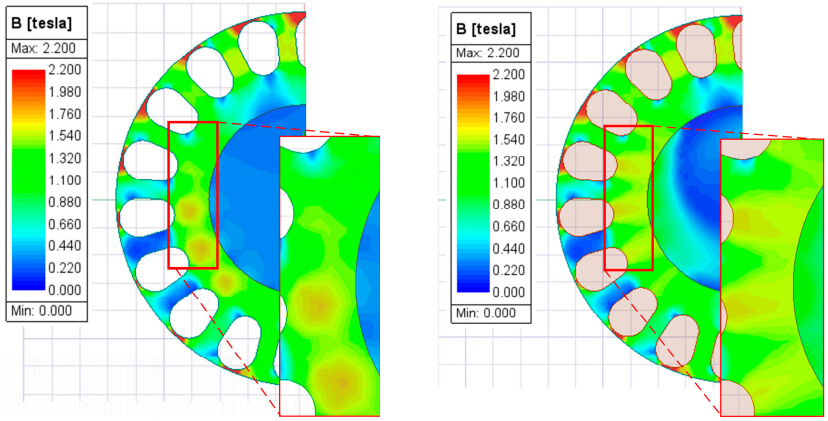

(**a**) (**b**)

Figure 3. The rotor back iron flux density distribution (**a**) without and (**b**) with eddy effects.

Therefore, the machine requires a higher magnetizing current to operate. As a result, the motor performance prediction deviates and creates errors with the classical IM equivalent circuit model since the input current and PF are calculated incorrectly [18,19].

The saturation due to the shaft eddy currents can possibly occur in high pole count IMs in case the magnetic loading level of the machine is high enough to saturate the rotor back iron [20]. A detailed study is presented in [19] showing the saturation occurring on four, and six-pole IMs' rotors. However, the saturation levels are found to be negligible when the pole count is higher.

3. Modified IM Equivalent Circuit

The classical IM equivalent circuit (CEC) is provided in Figure 4, where R_S is the stator phase resistance, X_{ls} is the stator leakage inductance, R_C is the core loss resistance, X_m is the magnetizing inductance, X'_{lr} is the rotor leakage inductance referred to the stator side, R'_R is the rotor resistance referred to the stator side, and s is the slip.

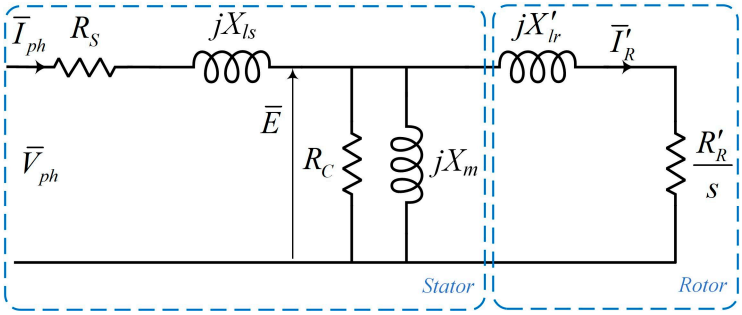

Figure 4. Classical IM equivalent circuit model.

The equivalent circuit parameters are determined through the DC, no-load, and locked rotor tests [21]. Since the magnetizing inductance is calculated when the machine is unloaded, the slip value is almost zero, and there are negligible small rotor and shaft currents.

As mentioned in Section 2, assuming the magnetizing inductance is not dependent on loading yields high estimation errors when modeling a two-pole IM.

Although the motor magnetizing inductance, X_m, is placed on the stator side of the equivalent circuit, its value is influenced by both stator and rotor. Hence, in this study, a modified equivalent circuit that takes both stator and rotor saturation into account is proposed. The modification is performed by adding a hypothetic rotor magnetizing inductance parallel to the stator magnetizing branch, along with a resistance added series to the rotor branch, as shown in Figure 5. Here, $X_{m,s}$ is the stator magnetizing inductance, $X'_{m,r}$ represents the inductance variation due to the magnetic saturation on the rotor back iron, $R_{sh,eddy}$ represents the rotor eddy current loss. This way, in the MEC, the main magnetizing inductance is considered to be a portion of the original X_m value, and the $X'_{m,r}$ value is a function of the slip, where the equivalent magnetizing inductance is equal to the original X_m that is experimentally measured or calculated through FEA under no-load conditions.

$$X_m = X_{m,s} // X'_{m,r}\big|_{s=0} = \left.\frac{X_{m,s} \times X'_{m,r}}{X_{m,s} + X'_{m,r}}\right|_{s=0} = X_m \tag{1}$$

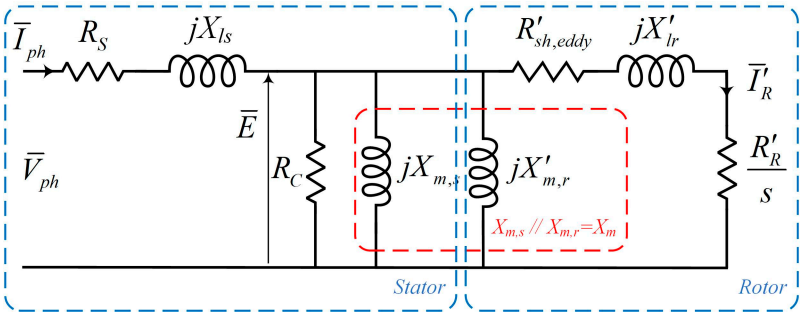

Figure 5. Modified IM equivalent circuit.

The behaviors of $X'_{m,r}$, and $X_{m,s}$ have to be understood to properly model them. According to the background information provided in Section 2, an increase in the load results in increased slip, which increases the rotor current frequency and amplitude. Consequently, shaft eddy currents increase, generating a repelling magnetic field on the rotor back iron that increases the saturation on the rotor back iron. Hence, the hypothetical rotor magnetizing inductance should vary with the slip, but due to the complexity of the problem, it is hard to determine the value and the variation of it. As a practical engineering approach, $X'_{m,r}$ is assumed to be a function that changes with the slip, where its variation speed with the slip and its minimum value is optimized based on the experimental measurements or FEA analysis. On the other hand, Equation (1) has to be satisfied when the slip is zero.

The $X_{m,s}$ value is defined as a constant portion of the measured X_m. This way, the machine magnetizing inductance will vary with the loading of the machine while considering rotor saturation due to the slip variation.

The expressions of $X'_{m,r}$ and $X_{m,s}$ are considered as follows.

$$X'_{m,r} = \left(\beta + (1-s)^{\alpha}\right) X_m \tag{2}$$

$$X_{m,s} = \gamma X_m \tag{3}$$

where β and α are the coefficients to be tuned based on the rotor saturation and slip. In Equation (3), γ is the coefficient of the $X_{m,s}$ that is a function of the parameter β that satisfies Equation (1). Since the parallel connection of $X_{m,s}$ and $X'_{m,r}$ is forming the magnetizing inductance itself, and the X_m value is measured or calculated at the unloaded condition, the expression in Equation (4) should be satisfied when the slip is zero. When Equations (2) and (3) are placed in Equation (1), the resulting expression can be written as in Equation (5).

$$\gamma X_m // X_m \left(\beta + (1-s)^{\alpha}\right)\big|_{s=0} = X_m \tag{4}$$

$$\left.\frac{\gamma\left(\beta + (1-s)^{\alpha}\right) X_m^2}{\left(\gamma + \beta + (1-s)^{\alpha}\right) X_m}\right|_{s=0} = X_m \tag{5}$$

Hence, the $X_{m,s}$ coefficient can be found as follows.

$$\gamma = \frac{(\beta + 1)}{\beta} \tag{6}$$

Since the frequency of the rotor currents is equal to the slip frequency, the eddy current loss is not significant. Hence, the $R'_{sh,eddy}$ is a small resistance, which is in some cases negligible small. If needed, the eddy current loss on the shaft can be calculated using the following expression.

$$P_{sh,eddy} = 3I'^2_R R'_{sh,eddy} \tag{7}$$

Although the effect of the $P_{sh,eddy}$ is small, results that present the machine performance become more precise.

4. Parameter Determination and Tuning

The classical equivalent circuit parameters of the machine can be determined through the DC, no-load, and locked rotor tests according to the standard IEEE test procedure [21]. Alternatively, one can find a clear and simplified equation with reasonable assumptions about equivalent circuit parameter determination in [22,23]. Newly introduced MEC parameters are calculated using the CEC parameters, experimental measurements at various loading conditions, and the parameter estimation system.

4.1. DC Test

The stator winding resistance is determined using the DC test, where various current values are passed through the windings using a variable DC source. During the test, the current and voltage values are recorded for resistance calculation. The test is performed as fast as possible to avoid temperature variations. The temperature also influences the resistance, where the resistance variance with the temperature can be expressed as follows [21].

$$R_{T_2} = \frac{R_{T_1}(T_2 + \alpha)}{T_1 + \alpha} \tag{8}$$

where R_{T_1} is the resistance value measured at the temperature T_1, R_{T_2} is the resistance value that is corrected for T_2 temperature, and α is the temperature coefficient of the material of the conductor.

4.2. No-Load Test

This test is performed when the machine is operated with no load connected to the shaft and with a balanced three-phase rated voltage applied to the windings. Here, the measured input power represents the summation of losses within the motor during no-load operation. These losses comprise stator I^2R (copper) losses, friction and windage losses, and core losses. There are two methods specified by IEEE standards for determining friction and windage losses. One approach involves subtracting the stator copper loss from the total losses at different test voltage points. After plotting the resulting power curve versus voltage, the point where it intersects with the zero-voltage axis provides the value for friction and windage loss.

The determination of friction and windage loss can alternatively be calculated by conducting a linear regression analysis utilizing three or more data points from the curve of power versus voltage squared [21].

$$P_{nl} = P_{cu} + P_{fw} + P_C \tag{9}$$

$$P_C = P_{nl} - (P_{fw} + P_{cu}) \tag{10}$$

where P_{nl} is the measured no-load power, P_{cu} is the stator copper losses, P_{fw} is the friction and windage losses, and finally, P_C represents the core losses.

4.3. Locked Rotor Test

The locked rotor test is performed to determine the rotor resistance and the summation of the stator and referred rotor leakage inductances. As the IM utilized in this study features a squirrel cage, its rotor incorporates a symmetrical bar winding. Consequently, the motor's impedance remains nearly identical regardless of the rotor's position relative to the stator [21]. During the experiments, voltage and current measurements are recorded at all phases, along with power input, at various voltage levels during the locked rotor test. Either the stator winding temperature or stator winding resistance needs to be recorded to ensure careful monitoring to prevent overheating of the windings. To balance the temperature, the highest readings should be observed first, and subsequently, the lower readings should be recorded. Upon generating the plots with volts on the x-axis and current, as well as input power on the y-axis, one can extract the voltage and power input values. These values are then used to calculate the total reactance, X_{ls} + $X'_{lr,}$ and rotor resistance, $R'_{R,}$ at the specified current level from the obtained curves.

The calculations start by assuming a relationship between X_{ls} and X'_{lr}. Since the mentioned squirrel cage IM is considered under Design A class by NEMA standards, the ratio between the X_{ls} and X'_{lr} is considered as 1, as specified in IEEE standards [21].

The next step is to determine the reactive power of the motor at no load, Q_{nl}, and at the conditions of the locked rotor test, Q_L.

$$Q_{nl} = \sqrt{(mV_{ph,nl}I_{ph,nl})^2 - P_{nl}^2} \tag{11}$$

$$Q_L = \sqrt{(mV_{ph,L}I_{ph,L})^2 - P_L^2} \tag{12}$$

$$V_{ph} = \frac{V_{ll}}{\sqrt{3}} \tag{13}$$

where m is the number of phases, $I_{ph,nl}$ is the measured no-load phase current, $V_{ph,nl}$ is the measured phased voltage during the no-load test and $V_{ph,L}$ is the phase voltage, $I_{ph,L}$ is the phase current, P_L is the power and during locked rotor test. V_{ph}, per phase voltage, is obtained as in Equation (13), where V_{ll} represents line-to-line voltage.

The magnetizing inductance X_m is calculated as in the following expression.

$$X_m = \frac{mV_{nl}^2}{Q_{nl} - (mI_{nl}^2 X_{ls})} \times \frac{1}{\left(1 + \frac{X_{ls}}{X_m}\right)^2} \tag{14}$$

Considering the test frequency, stator leakage reactance is determined as in Equation (15). Then, the same calculation is carried out at the rated frequency using Equation (16).

$$X_{ls,L} = \frac{Q_L}{mI^2{}_{ph,L} \times \left[1 + \left(\frac{X_{ls}}{X'_{lr}}\right) + \frac{X_{ls}}{X_{lm}}\right]} \times \left[\left(\frac{X_{ls}}{X'_{lr}}\right) + \frac{X_{ls}}{X_{lm}}\right] \tag{15}$$

$$X_{ls} = \frac{f}{f_L} \times X_{ls,L} \tag{16}$$

where $X'_{lr,L}$ is rotor leakage reactance at locked rotor test, f is the rated frequency, and f_L is the test frequency.

To determine the X'_{ls} and X_m, an iterative calculation method can be followed. First, Equation (14) can be solved for X_m by assuming the X'_{ls}/X_m, ratio, and X'_{ls} values. Second, Equation (15) is solved for $X'_{ls,L}$ using the assumed values in the first step, followed by solving Equation (16) for X'_{ls}. This procedure can be repeated by iterating the assumed values in the first step until a <0.1% error limit is achieved.

Similar to the stator leakage reactance, rotor leakage reactance at test frequency can be obtained by placing Equation (17) into Equation (18) as follows.

$$X'_{lr,L} = \frac{X_{ls,L}}{\left(\frac{X_{ls}}{X'_{lr}}\right)} \tag{17}$$

$$X'_{lr} = \frac{f}{f_L} \times X'_{lr,L} \tag{18}$$

The core loss resistance, R_C, can be obtained using the following equation.

$$R_C = \frac{1}{G_C} \tag{19}$$

$$G_C = \frac{P_C}{mV_{nl}^2} \times \left(1 + \frac{X_{ls}}{X_m}\right)^2 \tag{20}$$

Here, G_C is the core loss conductance in Siemens, and it is represented in Equation (20). P_C is the total core loss in watts, as determined in Equation (10).

Rotor resistance, R'_R, can be determined using the following expression [21].

$$R'_{R,L} = \left(\frac{P_L}{mI^2{}_{ph,L}} - R_{S,L}\right) \times \left(1 + \frac{X'_{lr}}{X_m}\right)^2 - \left(\frac{X'_{lr}}{X_{ls}}\right)^2 \times \left(X^2{}_{ls,L} G_c\right) \tag{21}$$

4.4. Power and Efficiency Calculations

According to IEEE standards, the efficiency is calculated using the following expression.

$$\eta = \frac{P_{out}}{P_{in}} = \frac{P_{out}}{P_{out} + P_{loss,total}} \tag{22}$$

Here, P_{out} is the mechanical output power that is calculated by the multiplication of the shaft speed and torque, P_{in} is the electrical input power, which can be calculated by adding the total power losses to the output power. The $P_{loss,total}$ is the total power loss that includes stator and rotor copper losses, $P_{cu,S}$ and $P_{cu,R}$, core loss P_C, rotational losses

obtained during the no-load test, and stray losses. Using the equivalent circuit, copper losses and core loss can be obtained with the following expressions.

$$P_{cu,S} = mI_{ph}^2 R_S \tag{23}$$

$$P_{cu,R} = mI'^2_R R_S \tag{24}$$

$$P_C = \frac{E^2}{R_C} \tag{25}$$

where E is the voltage across the core loss resistance.

The stray loss is separately calculated at different loading conditions by calculating the rest of the losses and subtracting them from the apparent total loss, which is the difference between the measured P_{out} and P_{in}. Once stray losses are determined at different loading conditions, they can be fitted to a curve that is a function of the square of the shaft torque.

The MEC also follows the same test procedure. As the magnetizing inductance value varies with the loading, resulting currents and voltages slightly vary, which affects the loss and efficiency calculation results. Since the proposed MEC parameters are tuned with the experimental test results, performance estimation becomes more accurate.

4.5. Modified Equivalent Circuit Parameter Determination

The CEC parameters can be determined by following the standard tests. Newly introduced equivalent circuit parameters, on the other hand, cannot be determined with the known methods but are estimated using loaded test measurements and an iterative parameter estimation method. To perform such estimation, the initial values of the new parameters should be selected carefully so that the results are not affected by their presence at the first estimation iteration. Hence, the initial value of the β is selected as 1, α is selected as 1, and consequently γ is calculated as 2 using Equations (1)–(6). This condition calculates the X_m value equal to the value that is determined by the no-load test. Using MATLAB's Parameter Estimation Tool, α and β values are tuned to minimize the error between the MEC model calculations and experimental results obtained at various slip conditions. During the estimation of β and α values, minimizing the error between data collected either from experimental or FEA is the objective of the parameter estimation system.

Evolutionary algorithms perform better than other algorithms, especially for electric machine optimization and parameter estimation tasks [24,25], in terms of the speed of the convergence and the quality of the final results. Algorithms like the genetic algorithm (GA) [26] and differential evolution (DE) [27] lie within the evolutionary optimization algorithm boundaries. In this work, the GA method is used to tune the new parameters of the modified equivalent circuit. Tuning is based on the errors of the power factor, motor current, and shaft torque between the experimental and equivalent circuit simulations. The general parameter estimation flow diagram is provided in Figure 6.

The estimation process starts with initializing three datasets, namely current vs. slip, power factor vs. slip, and shaft torque vs. slip from the experimental measurements or FEA simulations. These datasets are later compared with the equivalent circuit calculations, and errors are calculated to determine the optimization objective and generate the new parameters for the next iteration. In the second step, initialization of the equivalent circuit parameters determined in Section 3, the definition of the new MEC parameters' initial values and boundaries are made. The optimization objective is defined as the sums of the absolute values of the PF, I_{ph}, and the T_e. In the next step, the GA optimization is performed where, in each iteration, a set of parameters is generated, and the MEC is simulated with these parameters. The results are compared with the experimental results to calculate the optimization objective. The GA generates a new set of parameters based on the calculated cost. This operation continues until the termination criterion is reached.

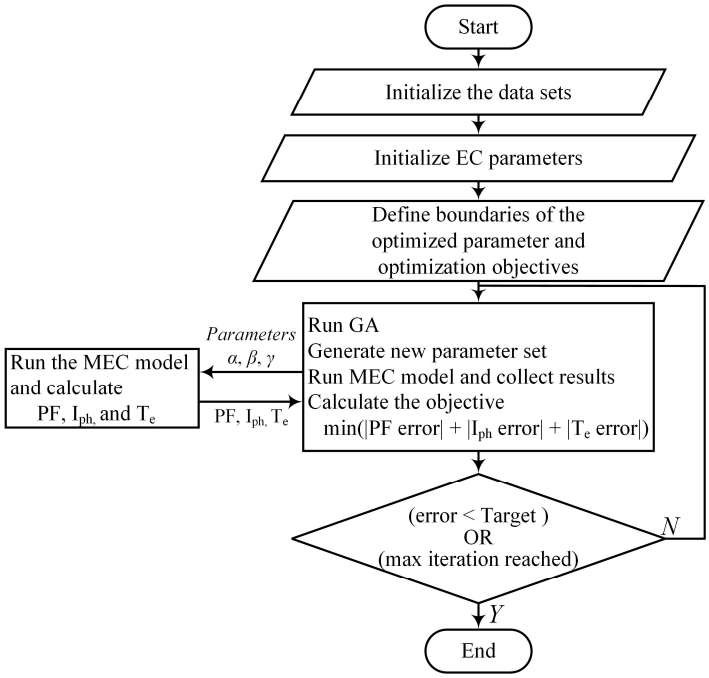

Figure 6. General flow diagram of the parameter estimation process.

MATLAB's (R2023a) Simulink Design Optimization Toolbox provides a straightforward parameter estimator graphical user interface that simplifies the parameter tuning process. The experimental results are compared with the simulated results and processed with the GA in the Simulink environment. The estimation is performed successfully, and convergence is achieved.

5. Results and Discussion

In this section, the IM CEC parameters are determined, the test system for loading tests is explained, and the parameter tuning results, MEC, FEA, and CEC model performance estimation comparisons are presented. Later, the analysis is extended for four different power-rating downhole pump motors to assess the validity of the proposed method.

5.1. Equivalent Circuit Parameter Determination

The IM modeling and parameter estimation procedure is performed on a two-pole 5.5 HP downhole pump motor, whose parameters are provided in Table 2.

Table 2. Motor parameters.

Parameter	Value
Power	5.5 HP
Number of Poles	2
Rated Voltage	400 V
Rated Current	9.82 A
Rated Speed	2826 rev/min
Rated PF	0.82
Rated Slip	5.79%

The equivalent circuit model simulation and parameter estimation study are performed in MATLAB/Simulink, while the FEA simulations are conducted in Ansys Maxwell. After the IM parameters are determined through locked rotor and unloaded tests, the IM equivalent circuit is built, and the IM performance is calculated for various loading conditions. The determined CEC parameters are provided in Table 3.

Table 3. Determined CEC parameters.

Parameter	Value
R_s	3.538 Ω
R'_R	1.115 Ω
$X_{ls} + X'_{lr}$	7.026 Ω
X_m	77.42 Ω
R_c	2460 Ω

5.2. Down Hole Pump Motor Test System

The tests are performed on the test system shown in Figure 7. The electrical input power, output torque, and speed signals are fed to a digital power analyzer for all the power and efficiency measurements.

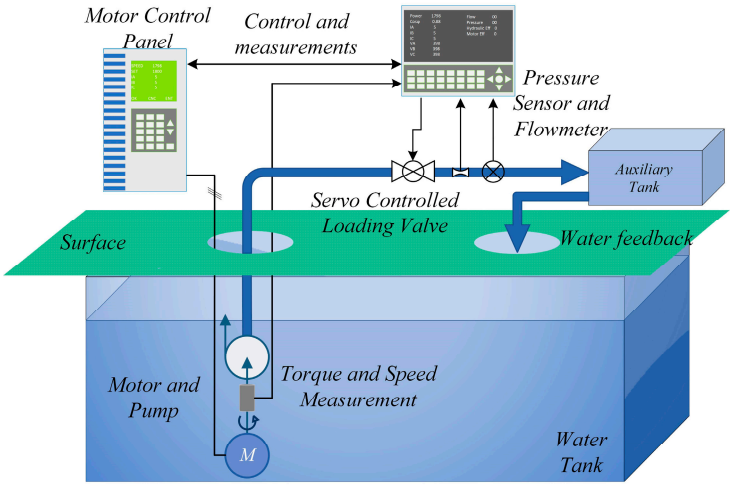

Figure 7. Downhole pump motor test system.

The testing system is not a usual dynamometer, which includes a loading motor coupled to the motor under test. The system includes a water pump coupled to the motor under test inside a water tank, where a torque sensor is inside a pressurized air chamber to prevent water from leaking inside the chamber. It is inserted between the motor and pump, as shown in Figure 8. Loading is performed by controlling the amount of water pumped outside with a servo-controlled valve. If the valve is fully closed, there is no water flow through the pump; hence, the loading is adjusted to its minimum value. As the valve is opened, water flows through the pump. The required torque to operate the pump at a certain speed is higher when there is a water flow, i.e., the amount of water flowing through the pump increases the required torque, and the pump motor loading is adjusted.

5.3. FEA Simulations

Before running the FEA simulations, determining the magnetic properties of the motor materials is important to achieve accurate results [28]. The motor lamination material is M400 electrical steel, and the shaft material is 1040 steel. As the shaft material's magnetic properties play a key role in accurate performance estimation, it has to be characterized before the FEA simulations. There are various methods to determine a solid ferromagnetic material's magnetic properties; some methods use electromagnets and Hall effect sensors [29], and some use classical BH loop measurements. In this study, the four-wire BH loop measurement method is used [7,30]. To perform the tests, a toroidal-shaped core is machined from the shaft material. Two windings are wound on the toroidal core. Table 4 shows the geometric parameters and the number of turn values of the toroid, Figure 9a shows the four-wire BH loop measurement test arrangement, and Figure 9b shows the toroid under test.

Figure 8. Motor under test, torque sensor, pump assembly, servo-controlled valve, pressure sensor, flowmeter, and auxiliary tank arrangement.

Table 4. Toroid Parameters.

Parameter	Value
Outer diameter	75 mm
Inner diameter	55 mm
Active length, l_{core}	204.2 mm
Cross-sectional area of the core, A_{core}	110.25 mm^2
Primary winding #of turns, N_1	160
Secondary winding #of turns, N_2	50
Density of the 1040 steel	7845 kg/m^3
Electrical resistivity of 1040 steel	17.1 µΩ/cm at 20.0 °C

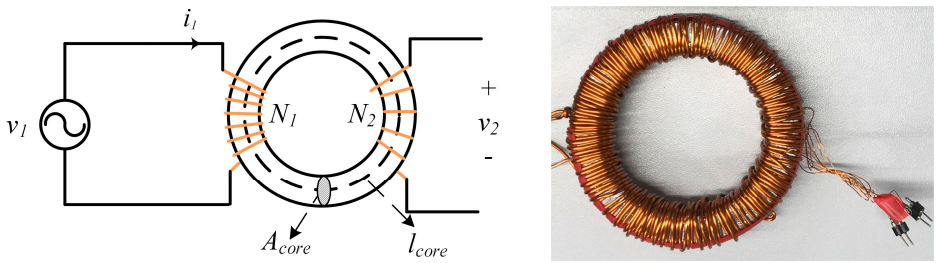

(**a**) (**b**)

Figure 9. (**a**) Four-wire BH loop measurement test arrangement and (**b**) the toroid.

In the four-wire BH loop measurement method, the second winding is used to sense the induced voltage and calculate the flux, ϕ, and flux density, B, in the core. The induced voltage on the secondary winding can be expressed as:

$$v_2(t) = N_2 \frac{d\phi(t)}{dt} = N_2 A_{core} \frac{dB(t)}{dt} \quad (26)$$

Hence, the flux density can be calculated by integrating the sensed secondary voltage $v_2(t)$.

$$B(t) = \frac{1}{A_{core} N_2} \int v_2(t) dt \tag{27}$$

The magnetic field intensity can be found using the following expression.

$$H(t) = \frac{N_1 i_1(t)}{l_{core}} \tag{28}$$

The test is conducted at a 50 Hz frequency with various input voltage amplitudes to vary the input current. Figure 10 shows the measurements, $v_1(t)$, $v_2(t)$, and $i_1(t)$, calculated $B(t)$ and $H(t)$ with Equations (26) and (27), and BH loops plotted after each consecutive measurement.

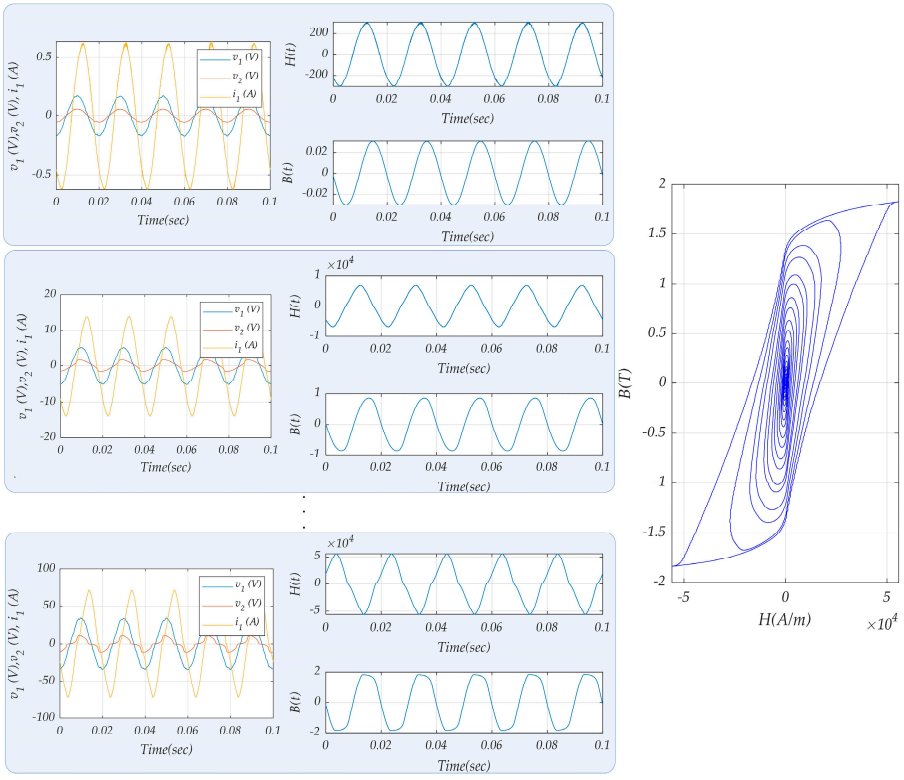

Figure 10. Four-wire BH loop measurements ($v_1(t)$, $v_2(t)$, and $i_1(t)$), calculated $B(t)$ and $H(t)$, and nested BH loops.

The resulting BH curve that is extracted from the peak points of the BH loops is presented in Figure 11. This curve is used in the FEA simulations.

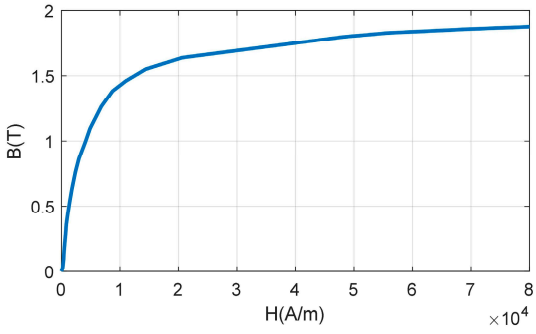

Figure 11. Measured BH curve.

Using FEA, the machine is simulated for several loading conditions, and performance metrics are recorded to be used for comparison.

5.4. Parameter Tuning

The parameter tuning is performed in MATLAB/Simulink by providing the PF error square sum over the range of zero to 14% slip range as an input to the MATLAB Parameter Estimation tool to tune the α, β, and $R_{sh,eddy}$ values to obtain the minimum error. Here, the experimental PF, input current, and torque data collected between the slip equals zero and 14% is used. The optimization algorithm is selected as GA, which has a maximum iteration number of 100. The system estimated the α, β, and $R_{sh,eddy}$ values as 252.3, 0.77, and 0.012, respectively.

5.5. Results Comparison

After the tuning process, optimized parameters are used in the MEC to estimate the test motor's performance, and results are compared with the test results along with the results of the CEC model and FEA simulation with and without eddy effects, which are presented in Figures 12–14.

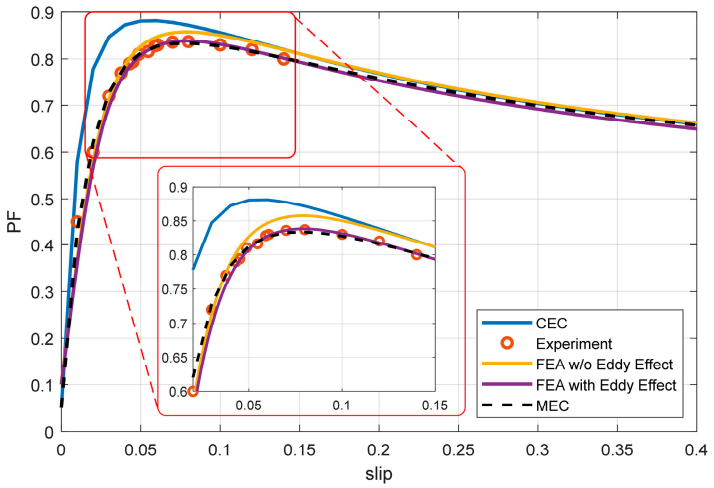

Figure 12. Estimated and measured PF comparison.

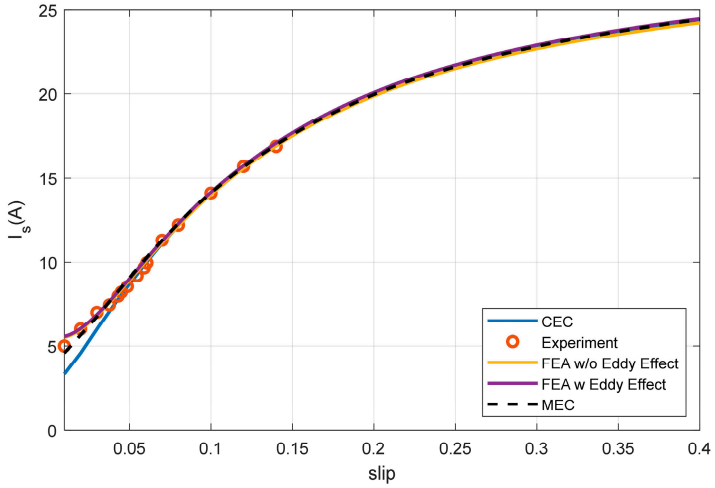

Figure 13. Estimated and measured current comparison.

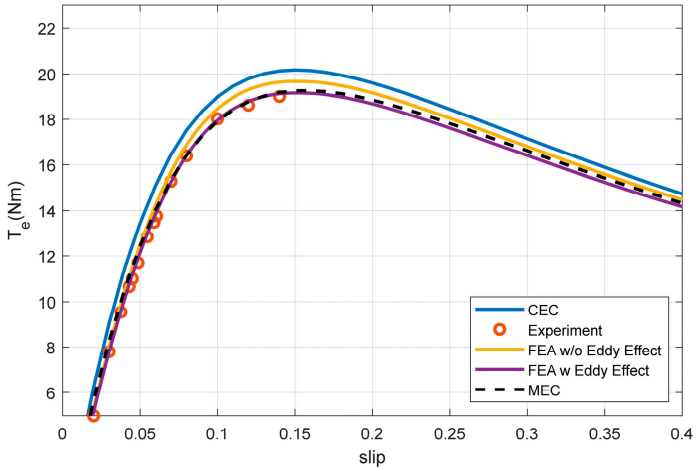

Figure 14. Estimated and measured torque comparison.

Figure 12 shows the PF variation versus the slip where the curves taken from CEC, experimental, FEA without eddy effect, FEA with eddy effect, and MEC are plotted on top of each other to highlight the differences. The experimental data are taken up to 1.4% slip value due to thermal constraints. Figure 12 also shows a zoomed view where the experimental measurement points exist. The CEC method yields the highest estimation error for PF, followed by the FEA, which does not consider the eddy effects. The FEA that takes eddy effects into account and the proposed MEC method produced the closest results with less than 0.5% error.

Figure 13 presents the line current measured experimentally and calculated using CEC, FEA, and MEC. The CEC again generates the highest error and deviates about 2.5% at the rated loading condition. The FEA simulations performed with and without eddy effects and MEC method accuracies are found to be similar for the experimentally measured operating region. The estimation error at the rated operating conditions is no more than 0.7% with the proposed method.

The torque calculations and measurements versus slip curves are provided in Figure 14. Similar to the other performance metrics, the CEC method overestimates the torque, too. FEA simulations with eddy effects were turned on, and MEC produced highly accurate results. The FEA simulation that does not consider eddy effects performs better than the CEC but still yields high errors at high torque regions.

Based on the results obtained for the 5.5 HP IM, the proposed rotor saturation branch happens to mimic the rotor back iron saturation caused by the increasing eddy currents with the loading [31].

To assess the validity of the proposed MEC technique, a set of two-pole downhole IM pump motors with different power ratings is considered. Table 5 presents the details of the motors tested for estimation performance comparison. It should be noted that the M1 shown in the first column is the 5.5 HP motor considered before.

Table 5. Motors under test.

Parameter	M1	M2	M3	M4	M5
Power (HP)	5.5	7.5	10	15	20
Rated Frequency (Hz)	50	50	50	50	50
Rated Voltage (V)	400	400	400	400	400
Rated Current (A)	9.82	12.71	16.97	24.3	33.6
Rated Speed (rev/min)	2826	2868	2890	2891	2898
Rated PF	0.843	0.825	0.828	0.821	0.810
Rated Slip (%)	5.79	4.41	3.68	3.63	3.43

The five motors provided in Table 5 are analyzed at their rated power conditions. Some important performance metrics, such as PF, current, and slip, are calculated and compared with the experimental measurements. A summary of the performance estimation errors is presented in Tables 6–9 for the PF, current, slip, and efficiency, respectively.

Table 6. PF percent error deviations with respect to the experimental results.

Machine Label	CEC	MEC	FEA w/Eddy Effect	FEA w/o Eddy Effect
M1	8.08%	0.37%	0.25%	2.57%
M2	7.39%	0.48%	0.24%	1.33%
M3	5.43%	0.60%	0.48%	1.93%
M4	5.85%	0.24%	0.12%	1.95%
M5	7.05%	0.25%	0.62%	1.98%

Table 7. Line current percent error deviations with respect to the experimental results.

Machine Label	CEC	MEC	FEA w/Eddy Effect	FEA w/o Eddy Effect
M1	2.5%	0.7%	0.2%	0.4%
M2	2.1%	0.4%	0.7%	0.2%
M3	1.8%	0.9%	0.5%	0.4%
M4	1.4%	0.2%	0.6%	0.2%
M5	1.7%	0.3%	0.4%	0.2%

Table 8. Slip percent error deviations with respect to the experimental results.

Machine Label	CEC	MEC	FEA w/Eddy Effect	FEA w/o Eddy Effect
M1	1.61%	0.36%	0.18%	0.71%
M2	1.13%	0.45%	0.68%	0.68%
M3	4.62%	0.82%	1.63%	2.45%
M4	2.48%	1.11%	1.11%	1.93%
M5	3.21%	0.58%	0.29%	1.46%

Table 9. Efficiency percent error deviations with respect to the experimental results.

Machine Label	CEC	MEC	FEA w/Eddy Effect	FEA w/o Eddy Effect
M1	2.11%	0.14%	0.28%	0.97%
M2	1.79%	0.29%	0.24%	1.52%
M3	1.17%	0.13%	0.29%	0.99%
M4	0.51%	0.13%	0.26%	0.39%
M5	0.37%	0.12%	0.04%	0.25%

Figure 15 presents the PF calculation and measurement results for the considered motors. At first glance, it can be noted that the CEC method overestimates the PF for all motors. FEA simulations without eddy effects also overestimated the PF but the difference is not as dramatically high as in the CEC case. The maximum error calculated for FEA simulations with eddy effects and MEC is 0.6%.

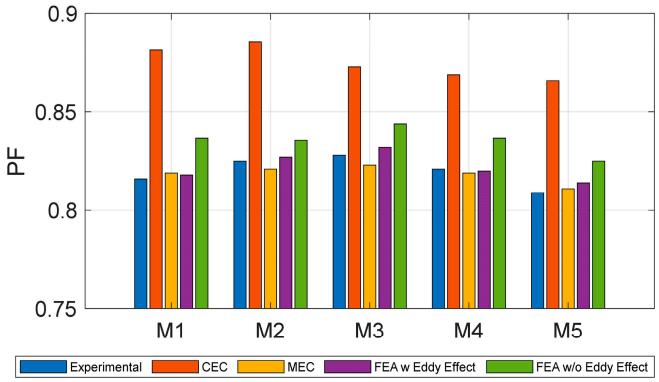

Figure 15. PF estimation comparison.

Current measurements and calculations using CEC, MEC, and FEA methods are presented in Figure 16. It should be noted that the per unit values are used in this figure for a clear presentation by taking experimentally measured values as base values. The CEC method consistently underestimates the input current, while both FEA methods with and without eddy effects slightly overestimate, and MEC performs similarly to the FEA simulations.

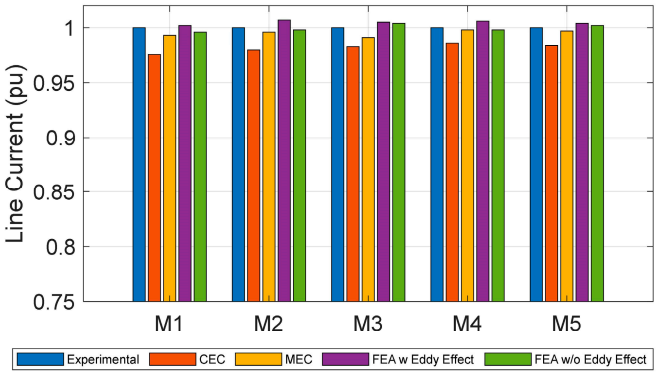

Figure 16. Line current estimation comparison.

Since the slip varies the rotor speed and torque, the rated output power can be achieved by adjusting the slip to the appropriate value. Hence, rather than comparing the output torque values, slip values are compared, as shown in Figure 17. The MEC method and FEA method with eddy effects perform better than other methods for all the motors. The CEC method again underestimates the slip, similar to the FEA simulation without eddy effects.

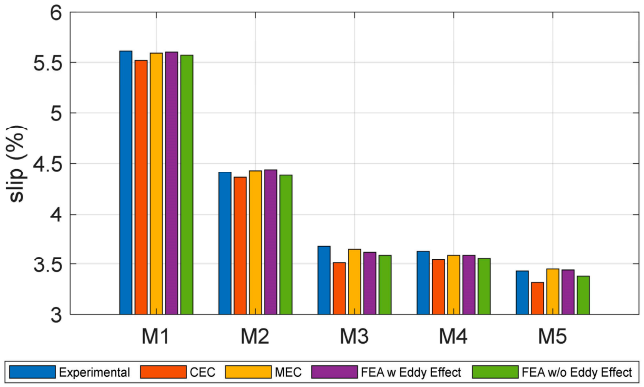

Figure 17. Slip estimation comparison.

Due to the deviations caused by saturation, the efficiency calculations exhibited slight variations. Figure 18 illustrates a comparison between the efficiency calculations and the experimental measurements. Calculations performed with the CEC and FEA without eddy effects tended to overestimate efficiency, whereas the MEC and the FEA with eddy effects resulted in higher accuracy for all the machines under test.

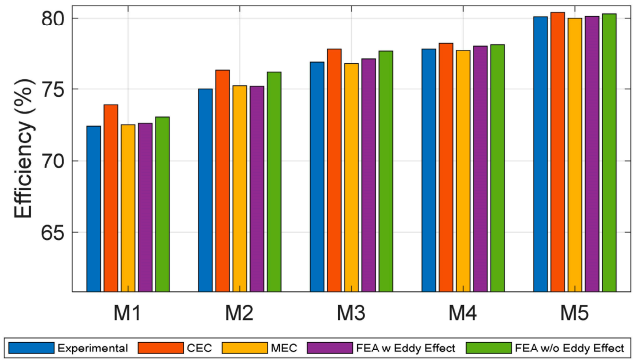

Figure 18. Efficiency estimation comparison.

To sum up, the shaft eddy current causes an additional saturation that affects the motor magnetizing inductance. This phenomenon can be observed through FEA simulations. The closest results are always obtained with the FEA simulations with eddy effects considered. However, the equivalent circuit model is usually the easiest and fastest way of motor performance estimation. Moreover, the CEC model is adopted by industry, and the determination of the motor parameters is standardized. Hence, equivalent circuit models are always preferred over FEA methods. According to the comparative study performed in this work, the proposed MEC method performs similarly to the FEA simulations and estimates the motor performance in a suitable correlation with the experimental measurements not only in the rated condition but over a wide operating range.

6. Conclusions

The classical equivalent circuit (CEC) parameters of induction machines (IMs) are determined through the standard no-load and locked rotor tests, where the magnetizing inductance value is calculated when the slip is close to zero. This approach usually does not yield high estimation errors for high pole count IMs. However, for the two-pole IMs, the main rotor flux not only travels through the rotor back iron but also goes through the shaft, which is made of a massive magnetic material. When the machine is loaded, the slip, the rotor current amplitude, and its frequency increase, which results in the shaft eddy currents on the axial direction of the machine increasing. The repulsive field that the eddy currents forces the rotor flux to flow through the rotor back iron but shaft. Therefore, the rotor saturation level increases. This phenomenon cannot be revealed with the unloaded condition tests; hence, the CEC model yields high estimation errors. This article introduces a modified equivalent circuit (MEC) with a new rotor saturation branch for the two-pole IM equivalent circuit to estimate the machine's performance accurately when the machine is loaded. The newly introduced parameters are tuned with a recursive estimation algorithm using the experimental test data. Later, the proposed MEC performance on estimating the power factor (PF), input current, rated power slip, and efficiency is compared with the CEC, FEA that considers eddy effects, and FEA without considering eddy effects. The proposed model and FEA with eddy effects closely correlated with the experimental measurement with less than 1% errors. Later, the study is extended to four additional motors at different power levels. Similarly, experimental results are well matched with the MEC and FEA with eddy effects. Considering that the equivalent circuit approximation generates results faster than any FEA simulation, the proposed method is superior in terms of the simulation speed while generating similar error percentages.

Funding: This research received no external funding.

Data Availability Statement: Data are contained within the article.

Acknowledgments: We would like to thank Mutlu Su Pumps and Motors for providing the motors and opening their test laboratories for my use for the experimental verification of this study.

Conflicts of Interest: The author declares no conflict of interest.

References

1. Lipo, T.A. *Introduction to AC Machine Design*; John Wiley & Sons, Inc.: Hoboken, NJ, USA, 2017; ISBN 9781119352181.
2. Kersten, A. Efficiency Investigation of Line Start Synchronous Reluctance Motors. Master's Thesis, Chalmers University of Technology, Göteborg, Switzerland, 2017.
3. Pyrhönen, J.; Jokinen, T.; Hrabovcová, V. *Design of Rotating Electrical Machines*; John Wiley & Sons: Hoboken, NJ, USA, 2008; ISBN 9780470695166.
4. Parrish, J.; Moll, S.; Schaefer, R.C. Synchronous versus Induction Motors. *IEEE Ind. Appl. Mag.* **2006**, *12*, 61–70. [CrossRef]
5. De Almeida, A.T.; Ferreira, F.J.T.E.; Baoming, G. Beyond Induction Motors—Technology Trends to Move up Efficiency. *IEEE Trans. Ind. Appl.* **2014**, *50*, 2103–2114. [CrossRef]
6. Oxley, P.; Goodell, J.; Molt, R. Magnetic Properties of Stainless Steels at Room and Cryogenic Temperatures. *J. Magn. Magn. Mater.* **2009**, *321*, 2107–2114. [CrossRef]
7. Tekgun, B.; Sozer, Y.; Tsukerman, I. Measurement of Core Losses in Electrical Steel in the Saturation Region under DC Bias Conditions. In Proceedings of the 2015 IEEE Applied Power Electronics Conference and Exposition (APEC), Charlotte, NC, USA, 15–19 March 2015; pp. 276–282.
8. Pedra, J.; Candela, I.; Barrera, A. Saturation Model for Squirrel-Cage Induction Motors. *Electr. Power Syst. Res.* **2009**, *79*, 1054–1061. [CrossRef]
9. Findlay, R.D.; Szabados, B.; Lie, S.; Spencer, S.; Belmans, R.; Poloujadoff, M. Placement of Vents to Reduce Shaft' Flux in Two Pole Induction Motors with a Comment on Heating Effects. *IEEE Trans. Energy Convers.* **1992**, *7*, 483–490. [CrossRef]
10. Tekgun, D.; Alan, I. A New Oval Shaft, High Performance, 2 Pole Line Start Synchronous Reluctance Machine for Submersible Pump Applications. *Int. J. Appl. Electromagn. Mech.* **2022**, *70*, 73–93. [CrossRef]
11. Tekgun, D.; Muhsin Cosdu, M.; Tekgun, B.; Alan, I. Investigation of the Effects of Multi-Layer Winding Structures in Two Pole Synchronous Reluctance Machines. In Proceedings of the 2021 IEEE 3rd Global Power, Energy and Communication Conference, GPECOM, Antalya, Turkey, 5–8 October 2021; pp. 120–125. [CrossRef]
12. Boglietti, A.; Cavagnino, A.; Lazzari, M. Computational Algorithms for Induction-Motor Equivalent Circuit Parameter Determination-Part I: Resistances and Leakage Reactances. *IEEE Trans. Ind. Electron.* **2011**, *58*, 3723–3733. [CrossRef]
13. Boglietti, A.; Cavagnino, A.; Lazzari, M. Computational Algorithms for Induction Motor Equivalent Circuit Parameter Determination-Part II: Skin Effect and Magnetizing Characteristics. *IEEE Trans. Ind. Electron.* **2011**, *58*, 3734–3740. [CrossRef]
14. Bianchi, N. Electrical Machine Analysis Using Finite Elements. In *Electrical Machine Analysis Using Finite Elements*; CRC Press: Boca Raton, FL, USA, 2017; pp. 1–275. [CrossRef]
15. Alberti, L.; Bianchi, N.; Bolognani, S. A Very Rapid Prediction of IM Performance Combining Analytical and Finite-Element Analysis. *IEEE Trans. Ind. Appl.* **2008**, *44*, 1505–1512. [CrossRef]
16. Park, G.J.; Son, B.; Seo, S.; Lee, J.H.; Kim, Y.J.; Jung, S.Y. Compensation Strategy of the Numerical Analysis in Frequency Domain on Induction Motor Considering Magnetic Flux Saturation. *IEEE Trans. Magn.* **2018**, *54*. [CrossRef]
17. Ojo, J.O.; Consoli, A.; Lipo, T.A. An Improved Model of Saturated Induction Machines. *IEEE Trans. Ind. Appl.* **1990**, *26*, 212–221. [CrossRef]
18. Dems, M.; Komeza, K.; Lecointe, J.P. Influence of Massive Ferromagnetic Shaft on the Distribution of Electromagnetic Field and Magnetising Current for Two- and Four-Pole Induction Motors at Frequencies of 50 and 200 Hz. *IET Electr. Power Appl.* **2018**, *12*, 1407–1416. [CrossRef]
19. Olivo, M.; Bortolozzi, M.; Tessarolo, A.; Luise, F. A New Method for the Accurate Prediction of On-Load Power Factor in Two-Pole Induction Motors Considering Shaft Eddy Currents. *IEEE Trans. Energy Convers.* **2020**, *35*, 1196–1207. [CrossRef]
20. Ben Slimene, M.; Khlifi, M.A. Investigation on the Effects of Magnetic Saturation in Six-Phase Induction Machines with and without Cross Saturation of the Main Flux Path. *Energies* **2022**, *15*, 9412. [CrossRef]
21. *112-2017*; IEEE Standard Test Procedure for Polyphase Induction Motors and Generators. IEEE: Piscataway, NJ, USA, 2018.
22. Boldea, I.; Nasar, S.A. *The Induction Machines Design Handbook*; CRC Press: Boca Raton, FL, USA, 2018; ISBN 9781315222592.
23. Umans, S.D. *Fitzgerald and Kingsley's Electric Machinery*, 7th ed.; McGraw-Hill: New York, NY, USA, 2014; ISBN 9780073380469.
24. Tekgun, D.; Tekgun, B.; Alan, I. FEA Based Fast Topology Optimization Method for Switched Reluctance Machines. *Electr. Eng.* **2022**, *104*, 1985–1995. [CrossRef]
25. Shao, H.; Zhong, C.; Habetler, T.G.; Li, S. Multi-Objective Design Optimization of Synchronous Reluctance Machines Based on the Analytical Model and the Evolutionary Algorithms. In Proceedings of the 51st North American Power Symposium, NAPS 2019, Wichita, KS, USA, 13–15 October 2019. [CrossRef]

26. Benlamine, R.; Dubas, F.; Randi, S.A.; Lhotellier, D.; Espanet, C. Design by Optimization of an Axial-Flux Permanent-Magnet Synchronous Motor Using Genetic Algorithms. In Proceedings of the 2013 International Conference on Electrical Machines and Systems, ICEMS 2013, Busan, Republic of Korea, 26–29 October 2013; pp. 13–17. [CrossRef]
27. Storn, R. Differential Evolution—A Simple and Efficient Heuristic for Global Optimization over Continuous Spaces. *J. Glob. Optim.* **1997**, *76*, 341–359. [CrossRef]
28. Costa, L.F.T.; de Campos, M.F.; Gerhardt, G.J.L.; Missell, F.P. Hysteresis and Magnetic Barkhausen Noise for SAE 1020 and 1045 Steels with Different Microstructures. *IEEE Trans. Magn.* **2014**, *50*, 2001504. [CrossRef]
29. Gao, Y.; Naoki, Y.; Zhao, H.; Gotoh, Y.; Guan, W.; Muramatsu, K. Investigation on Magnetic Property Measurement Method of Solid Specimens Using an Electromagnet. In Proceedings of the 2022 25th International Conference on Electrical Machines and Systems (ICEMS), Chiang Mai, Thailand, 29 November–2 December 2022; pp. 1–4.
30. Tekgun, B.; Boynuegri, A.R.; Chowdhury, M.A.M.; Sozer, Y. Design and Implementation of a Sinusoidal Flux Controller for Core Loss Measurements. In Proceedings of the 2016 IEEE Applied Power Electronics Conference and Exposition (APEC), Long Beach, CA, USA, 20–24 March 2016; pp. 207–214.
31. Poltz, J.; Kuffel, E. A Simple and Accurate Evaluation of Eddy-Current Loss in Magnetic Pipe of a Cable. *IEEE Trans. Power Appar. Syst.* **1985**, *PAS-104*, 1951–1957. [CrossRef]